Adaptive bone re-modelling for optimization of porous structural components

(article starts on next page)

Adaptive bone re-modelling for optimization of porous structural components

Jens OLSSON*, Mats ANDER[ab], Chris J. K. WILLIAMS[b]

* Department of Architecture and Civil Engineering
Chalmers University of Technology
412 58 Gothenburg, Sweden
jens.olsson@chalmers.se

[a] Chalmers University of Technology, Dep. of Industrial and Material Science
[b] Chalmers University of Technology, Dep. of Architecture and Civil Engineering

Abstract

This paper presents a speculative application of adaptive bone-remodelling to generate porous structures for building components using a numerical meshless method. We hypothesize that such porous structures could then be 3d printed to achieve light weight and material efficient building components. The meshless model is built up with particles that are connected by arms to their neighbours withing a distance called a horizon. The re-modelling adaption is then base on the ration of arms strain over average arm strain which is mapped to a third order polynomial function and used to scale the arm stiffness in a way that mimics the resorption and densification of bone tissue. The method is shown to work rather well in the recreation of the structural patterns found in cross section of a femur bone. The translation to a geometry which can be manufactured with additive techniques is not tackled specifically and suggest a direction for further work.

Keywords: Meshless methods, bone re-modelling, structural design, optimisation, porous structures.

1 Introduction

Computational tools in architecture and engineering aim to support the designer with information that can be used to guide the distribution of matter in the formation of spaces and structures. Since the early days of computational design, the range of application has broadened from structural design, energy calculations to manufacturing and even space planing. Recent development of computational power has broaden the scope for digital models from detailed simulations of small material constituents to digital twins of entire cities. Although the application of computation to the simulation of material behaviour, flow of wind in a city planning context or the movement people may seem completely different, the underlying mathematics can be quiet similar. The work presented in this paper is part of a broad exploration of digital tools within the Digital Twin Cities Centre project at Chalmers university of technology [1], looking specifically at the interplay between design and structural analysis.
In this paper we strive to present a simple mathematical model that can be used to guide placement of material in a structural engineering design situation. The results form the simulation

can also be interpreted quiet literally in the design of porous structures. Although the translation from a meshless model (consisting of the particles and arms) into a 3D form, is not dealt with specifically in this paper.

The proposed method builds on the simplest form of a meshless method where the continuum domain is discretised using particles that are interconnected with spring-like elements that will be referred to as arms. The stiffness of the arms are varied based on the principles found in Bone re-modelling so that more strained areas become stiffer and less strained areas are weakened.

A range of methods have been proposed to enable a similar material guidance in structural design. Among which, various forms of topology optimisation [2], different forms of truss optimisation, as exemplified in [3] base on the interior point method, in [4] based on graphical rules, and in [5] applied in real structural design situations.

1.1 Bone re-modelling

Bone tissue has been found to reconfigure its structural morphology as a response to external stimuli. This process which today is referred to as adaptive bone-remodelling was first discovered by Wolff in 1892 [6] and postulated in what is called Wolff's law which say that

> *In a mature bone where the general form is established, the bone elements place or displace themselves, and decrease or increase their mass, in response to the mechanical demands imposed on them.*

A diverse set of mathematical models have since been proposed to recreate the bone growth behaviour that is observed in nature. The models are typically based on mechanical stimuli derived from measures of strain, stress or energy and the 'adaptive elasticity' model based on the measure of strain energy density (SED) by Huiskes [7] has gained notable popularity in this field of research. An overview for the use of the SED methods is given in [8]. Adaptive bone re-modelling has been applied to model screw implants and the in-growth of bone into implant cavities [9]. A study from 2000 approach the modelling of internal bone structure of a proximal femur as an optimisation process [10], and others have explored the similarities of bone re-modelling and topology optimisation [11]. The first use of meshless methods to simulate adaptive bone re-modelling was published in [12].

1.2 Meshless methods

Smoothed Particle Hydrodynamics (SPH) was introduced by Gingold and Monaghan in 1977 and is usually referred to as the first meshless method [13]. It was developed for modelling of astrophysics phenomena but has been widely adopted in modelling of fluids for complex flow situations, including fluid structure interaction. The grid free nature of SPH makes it suitable for modelling of large deformations, for example in the context of rock mechanics and geoengineering but also in manufacturing related processes that involve large deformation of solids, for example extrusion and forging of metals.

Peridynamics is another meshless method that was introduce in 1999 for the simulation of fracture [14]. The continuum domain is discretised by a set of particles which are connected to their neighbours through a set of arms spanning a distance which is called the horizon. Since the arms reach further than their immediate neighbours, it is just like SPH referred to as non-local method, and is therefor an appropriate approach for modelling of stress concentrations and progressive fracture.

2 Model setup

Several strategies can be used to set up a particle model for analysis. The fundamental problem concerns populating a domain in 2D or 3D with particles and structuring the data in a way to enable performance efficient calculations. A strategy also need to be chosen for how to define the domain of interest, preferably in a way that enables efficient point inclusion calculations. For the 2D case, a polyline can be used to define the material body, and the point inclusion calculations can be carried out using a line intersection principle. Given a point that is located within the bounding box $([X_{min}, X_{max}], [Y_{min}, Y_{max}])$ of a container polyline, a horizontal line is drawn from the point to the maximum x-vaule of the bounding box. If the line intersects with the polyline at an odd number of instances, the point lies inside the polyline.

For the 3D case, a volumetric mesh of tetrahedral elements can be used to define the object. The inclusion of a point inside the elements of the volume mesh can be done by reformulating the coordinates for the point in the barycentric coordinates for each tetrahedron. If and only if all the barycentric coordinates $(x_1, x_2, x_3, x_4) > 0$, the point lays inside the tetrahedral element. Each point is then tested for the appropriate proximal tetrahedral elements to conclude inclusion or exclusion in the object.
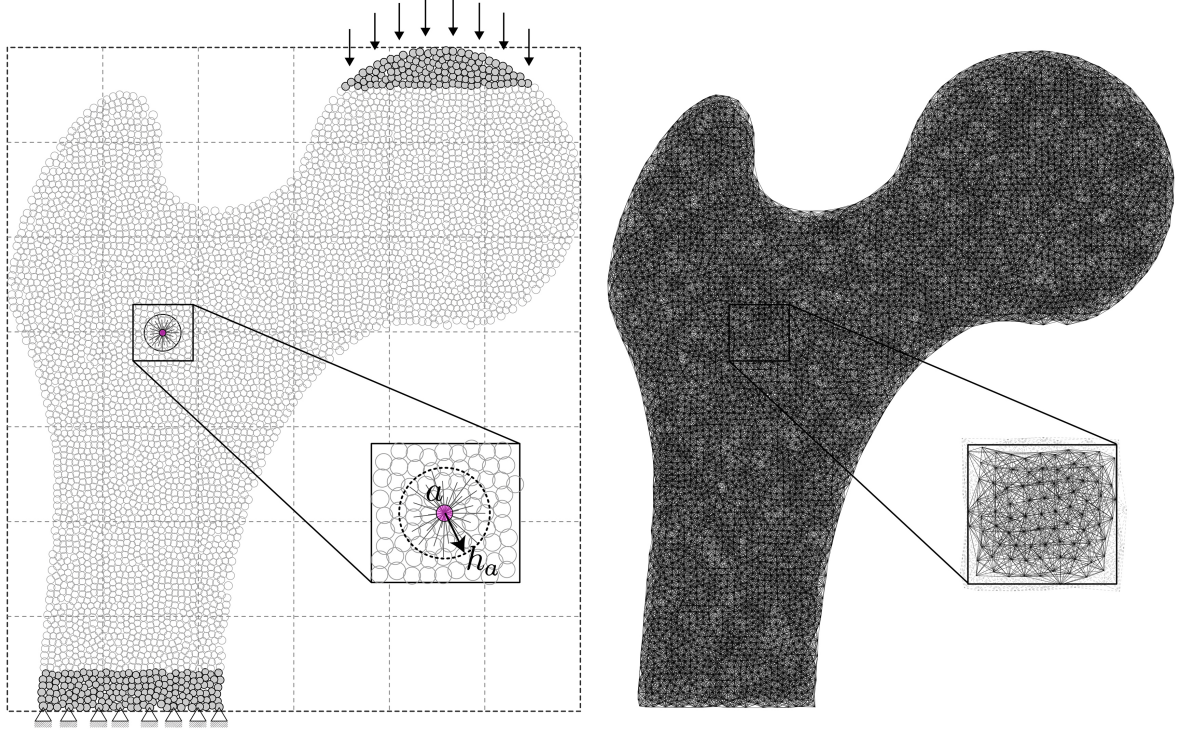

Figure 1: Setup of a 2D femur with the particle arrangement and boundary conditions to the left and the resulting network of arms to the right. A particle **a** within the horizon h_a for $\alpha = 5.5$ is highlighted in the selected region.

Using said strategies for domain definition and point inclusion calculation, a regular grid of particles can be generated by discritising the bounding box $([X_{min}, X_{max}], [Y_{min}, Y_{max}], [Z_{min}, Z_{max}])$ of the object with a spacing $(\Delta x, \Delta y, \Delta z)$. The bounding box is furthermore divide into a grid

of zones, which can be seen in Figure 1. Each particle is associated to a zone index, which can be calculated from the coordinates of the particle, the zone step size and the bounding box size. Such zone indexing are standard procedure in particle simulations with SPH och discrete particle models.

To simplify the setup we may assume that all the particles a have the same size which is calculated by dividing the area of the whole object with the number of particles. From the particle area, the particle radius r_a can be retrieved, assuming that the particles are circular. The horizon h_a for a particle is then calculated from $h_a = r_a \alpha$, where α is a parameter of choice. The next step of the setup involves the option to introduce noise in the particle distribution through a type of shaking procedure. The algorithm which is used in this paper for that purpose can be found in [15] section 10.2. Following the introduction of noise, the particle setup is established and the arms need to be created. This is done by connecting each particle a with all the neighbouring particles b within the horizon of a.

3   A simple meshless model

The simplest form of a meshless method consists of particles that are interconnected with spring-like arms as described in section 2 and shown in Figure 1. For the same setup of particles a variety of phenomena can be modelled based on the introduction of different particle interaction conditions or force laws. In this context a simple linear elastic material will be modelled where the arm force is based on the strain of the arms and the arm stiffness.
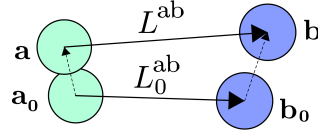

Figure 2: Two particles in their initial position $\mathbf{a}_0, \mathbf{b}_0$ and deformed position $\mathbf{a}, \mathbf{b}$ respectively.

The arm strain ϵ_{ab} is calculated from

$$\epsilon_{\mathrm{ab}} = \frac{L^{\mathrm{ab}} - L_0^{\mathrm{ab}}}{L_0^{\mathrm{ab}}}, \tag{1}$$

where L^{ab} is the deformed length of the arm and L_0^{ab} is the initial arm length. The arm-force T_{ab} is then calculate from

$$T_{\mathrm{ab}} = \epsilon_{\mathrm{ab}} \frac{S}{L_0^{\mathrm{ab}}}, \tag{2}$$

where S is the arm stiffness. The total force on a particle a surrounded by n number of neighbours then becomes

$$\mathbf{f}_{\mathrm{a}} = \sum_{\mathrm{b}}^{\mathrm{b}=n} \epsilon_{\mathrm{ab}} \frac{S}{L_0^{\mathrm{ab}}} \mathbf{q}_{\mathrm{ab}} + \mathbf{g}, \tag{3}$$

where $\mathbf{f}_{\mathrm{a}}$ is a vector with the force components in [N], $\mathbf{q}_{\mathrm{ab}}$ is the unit direction vector from particle a to particle b calculated from $\mathbf{q}_{\mathrm{ab}} = (\mathbf{b} - \mathbf{a}) / |\mathbf{b} - \mathbf{a}|$, and $\mathbf{g}$ is the body load vector in [N]. From this a simple starting point, more elaborate mechanical properties can be introduced in the formulation of the arm-force, to capture more complicated phenomena. One such example is shown with the modelling of fracture in [15], where the arm-force is based on the concept of force flux density enabling spontaneous fracture for a material with an arbitrary Poisson's ratio.

3.1 Adaptive stiffness

The stiffness adaptation is achieved by scaling the stiffness for the arms, and the scale factor is driven by the ratio of arm strain over average arm strain. The average arm strain k is calculated though a summation of all the arm strain divided by the number of arms n such that

$$k = \sum_{i=0}^{i=n} \frac{\epsilon_i}{n}. \tag{4}$$

The stiffness scale factor β is derived with inspiration from bone re-modelling principles where different parts of the bone structure are either in resorption, in densification or in a type of dormant mode. The typical stimuli-densification graph from bone re-modelling is approximated here with a function δ, which is based on a third order polynomial, as shown in Figure 3. Two additional polynomials are also included, to exemplify how the width of the plateau and the steepness of densification and resorption can be altered by just changing the order of the polynomial. The stiffness scale factor β is calculated from

$$\beta_{\mathrm{ab}} = 1 + \delta(\epsilon_{\mathrm{ab}}, k), \tag{5}$$

where δ is defined as

$$\delta_{\mathrm{ab}} = \left(\frac{\epsilon_{\mathrm{ab}}}{k} - 1 \right)^3, \tag{6}$$

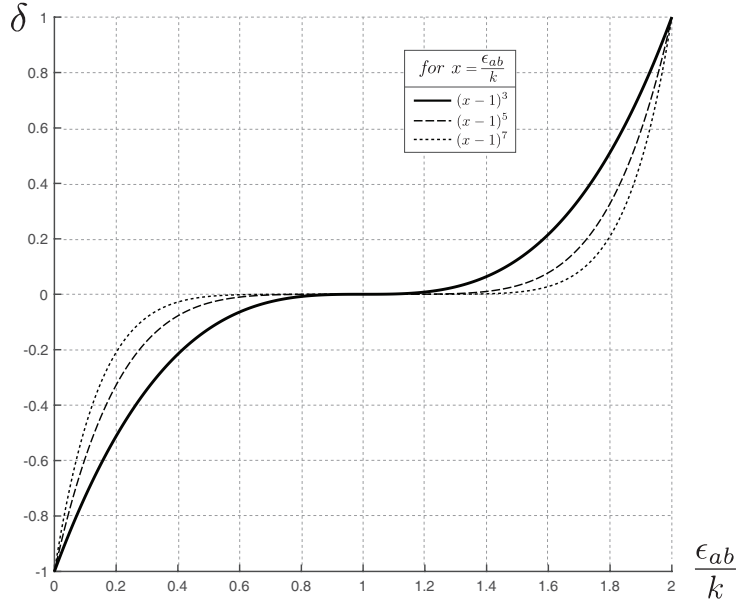which can be seen in Figure 3. In order to slow down the growth of stiffness and to allow the

Figure 3: Three different equations that can be used to modify the stiffness of the arms based on the strain over average strain ratio. The third order polynomial represented by the continuous curve has been used for the examples in section 4.

model to find and adapt to new load paths, the δ component is incremented iteratively, and multiplied with a scaling damping factor γ. The introduction of γ also becomes an opportunity

to control the rate of resorption and densification to ensure stability and convergence. The incremental formulation of δ, following the time stepping in section 3.2, thus becomes

$$\delta_{\mathrm{ab}}^t = \delta_{\mathrm{ab}}^{t-\Delta t} + \gamma \left(\frac{\epsilon_{\mathrm{ab}}^t}{k} - 1 \right)^3, \tag{7}$$

assuming that $\delta_{\mathrm{ab}} = 0$ at $t = 0$. The scale damping γ is defined as

$$\gamma = \begin{cases} 0.0005 & \text{if, } \dfrac{\epsilon_{\mathrm{ab}}}{k} > 1 , \\ 0.001 & \text{if, } \dfrac{\epsilon_{\mathrm{ab}}}{k} < 1 , \end{cases} \tag{8}$$

resulting in a slower densification and faster resorption. Additional limit conditions on the total stiffness scaling factor can be applied such that $\beta_{min} \leq \beta_{\mathrm{ab}} \leq \beta_{max}$. Where β_{min} is typically $1/100$ if $\beta_{max} = 100$. The values for $\gamma, \beta_{min}, \beta_{max}$ will need some tailoring for each specific problem depending on the overall stiffness in the structure, the loading rate etc. The arm force from Eq.(2) is then updated to become

$$T_{\mathrm{ab}} = \beta_{\mathrm{ab}} \epsilon_{\mathrm{ab}} \frac{S}{L_0}. \tag{9}$$

The total force on a particle a surrounded by n number of neighbours as shown in in Eq.(3) then becomes

$$\mathbf{f}_{\mathrm{a}} = \sum_{\mathrm{b}=0}^{\mathrm{b}=n} \beta_{\mathrm{ab}} \epsilon_{\mathrm{ab}} \frac{S}{L_0^{\mathrm{ab}}} \mathbf{q}_{\mathrm{ab}} + \mathbf{g}. \tag{10}$$

3.2 Solver procedure

In order to solve Eq.(10) for a specific particle model an explicit time integration scheme can be used to calculate the acceleration, velocity and displacements by stepping through time. The stiffness scaling is then initiated once the modelled has reached a convergent force distribution. The procedure starts with an initial undeformed geometry at time $t = 0$ and initial velocities equal to zero at time $t = -\Delta t/2$. A time step Δt is chosen, the displacements are then evaluated at $t = 0$, $t = \Delta t$, $t = 2\Delta t$... and the velocities are evaluated at the half steps $t = -\Delta t/2$, $t = \Delta t/2$, $t = 3\Delta t/2$... The time stepping follows the 'leapfrog' technique, which is somewhat simpler than Verlet integration[16], and after N cycles the amount of time t that has passed is $t = N\Delta t$. At each cycle the strain is calculated from Eq.(1), δ_{ab} from Eq.(7), β_{ab} from Eq.(5) and the total force on a particle $\mathbf{f}_{\mathrm{a}}$ from Eq.(10). The acceleration of the particle is calculated by dividing the total force on the particle by its fictitious mass such that

$$\mathbf{A}_{\mathrm{a}}^t = \frac{\mathbf{f}_{\mathrm{a}}^t}{\mathbf{m}_{\mathrm{a}}^t}, \tag{11}$$

where the fictitious mass $\mathbf{m}_{\mathrm{a}}^t$ is calculated from the accumulated arm stiffness such that,

$$\mathbf{m}_{\mathrm{a}}^t = \sum_{\mathrm{b}=0}^{\mathrm{b}=n} \beta_{\mathrm{ab}}^t \frac{S}{L_0} \mathbf{q}_{\mathrm{ab}}^t. \tag{12}$$

The velocity at the next half step is calculated using,

$$\mathbf{V}_{\mathrm{a}}^{t+\Delta t/2} = c\mathbf{V}_{\mathrm{a}}^{t-\Delta t/2} + \Delta t \mathbf{A}_{\mathrm{a}}^t, \tag{13}$$

where a carry over factor c is introduced as fictitious damping of the velocity from previous iteration. The optimal value is chosen empirically, with typical values in the range 0.99 to 0.999. It should be noted that if we wanted to model viscous damping accurately then we would set $c = 1$ and we would need to estimate $\mathbf{V}_a^t$ in order to include the damping force term in $\mathbf{A}_a^t$. The new displaced position for a particle is then calculated from the previous position $\mathbf{X}_a^t$ and the velocity from Eq.(13) using

$$\mathbf{X}_a^{t+\Delta t} = \mathbf{X}_a^t + \Delta t \mathbf{V}_a^{t+\Delta t/2}. \tag{14}$$

This is the end of the cycle and the time is the incremented to,

$$t = t + \Delta t, \tag{15}$$

and the procedure repeated.

3.3 Boundary conditions

Compared to classical continuum mechanics and the Finite element method (FEM), the setup of the boundary condition for a meshless method works a bit different. Since meshless methods are typically non-local methods (the particles are connected to more then just the closest neighbours) the boundary conditions should be applied to a layer of particles with a depth that is at least as large as the largest horizon in that area. Whereas the natural boundary condition if FEM is a traction force, the boundary force in peridynamics is a force density applied at some depth beyond the surface layer. Similarly, displacement boundary conditions are prescribed within a layer of finite thickness under the surface [17].

4 Results

In this section the results from a set of different applications are presented. The fist case is the classical femur model which is a standard simulation in bone re-modelling research. The second case is a 3D version of the femur and finally a 2D application for a structural frame is presented. The implementation is done using C++ and the visualisation is done with OpenGL.

4.1 Femur 2D

The 2D cross section of a femur bone as shown in Figure 1 is populated with 4986 particles resulting in 137427 arms when the particles are connected with their neighbours for $\alpha = 5.5$. The load is applied on top of the femoral head pointing in the direction of the arrows in Figure 1 to mimic the load transfer form the pelvis to the femur for a standing person. The shaft of the femur is furthermore locked in place as illustrated in Figure 1. The distribution of compression and tension in femur prior to the stiffness scaling can be seen in Figure 4a, and the total strain on the particles can be seen in Figure 4b. The distribution of stiffness scaling β for the femur can be seen in Figure 5.
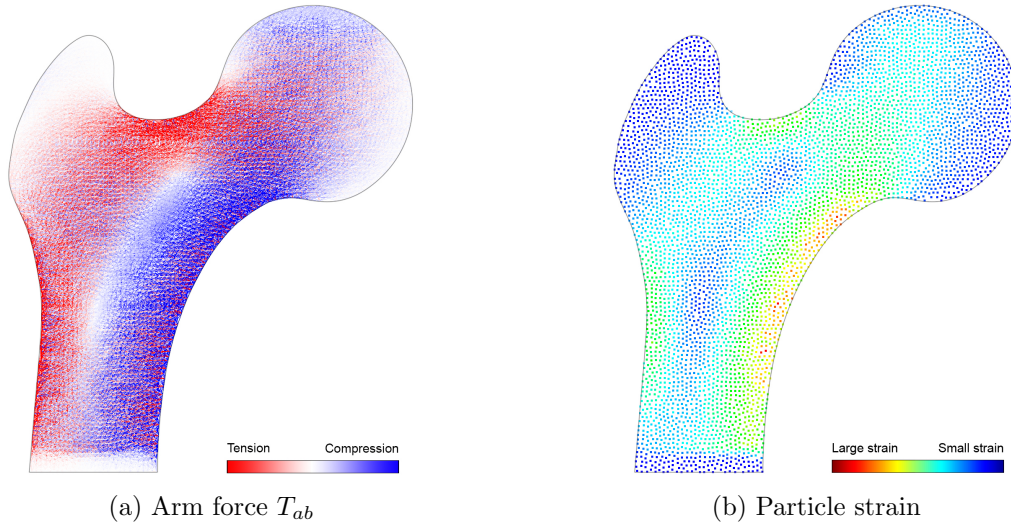
(a) Arm force T_{ab}
(b) Particle strain

Figure 4: Analysis results for the 2D femur from prior to stiffness scaling. The tension and compression force follows the expected distribution from a bending situation.
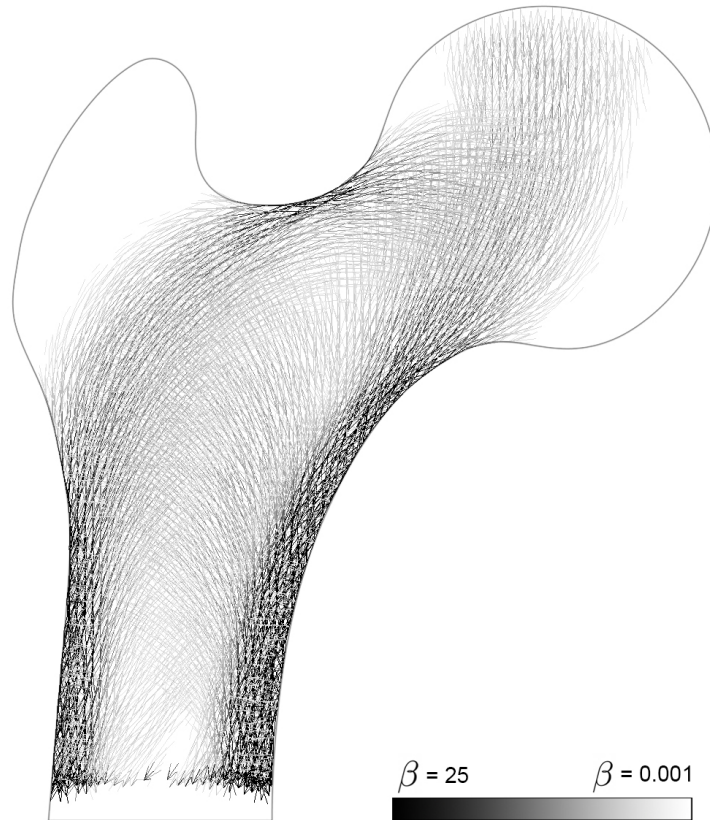

Figure 5: The 2D femur bone where the arms colored by the stiffness scale factor β_{ab}. Black arms are stiff and white arms a weak.

4.2   Femur 3D

The second example is an extension of the 2D bone in section 4.1 to 3D. A scanned femur is approximated with a volume mesh and populated with 23852 particles, where barycentric coordinates are used for inclusion calculations as described in section 2. The bone is locked at the base of the shaft with a depth larger than the largest particle horizon. An incremental load is applied to the top of the bone to mimic the weight of a standing person. For $\alpha = 4.5$ each particles is connected to an average of 76 neighbours and the total number of arms are 1816662.
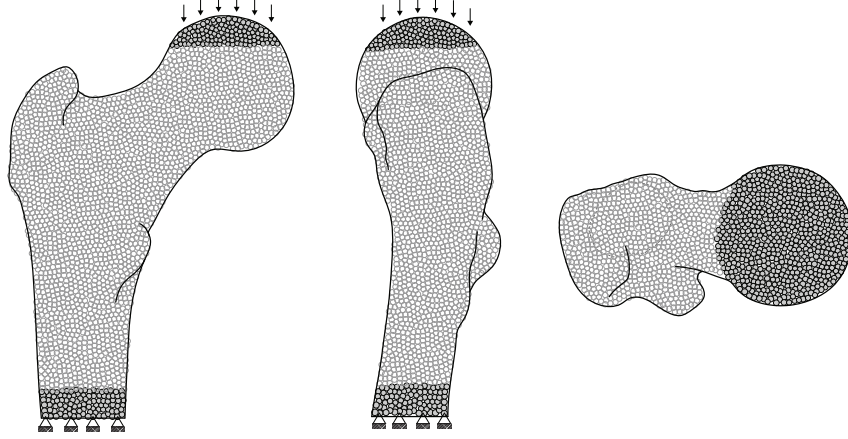
Figure 6: Setup of the femur bone model in 3D with two elevations and a top view.

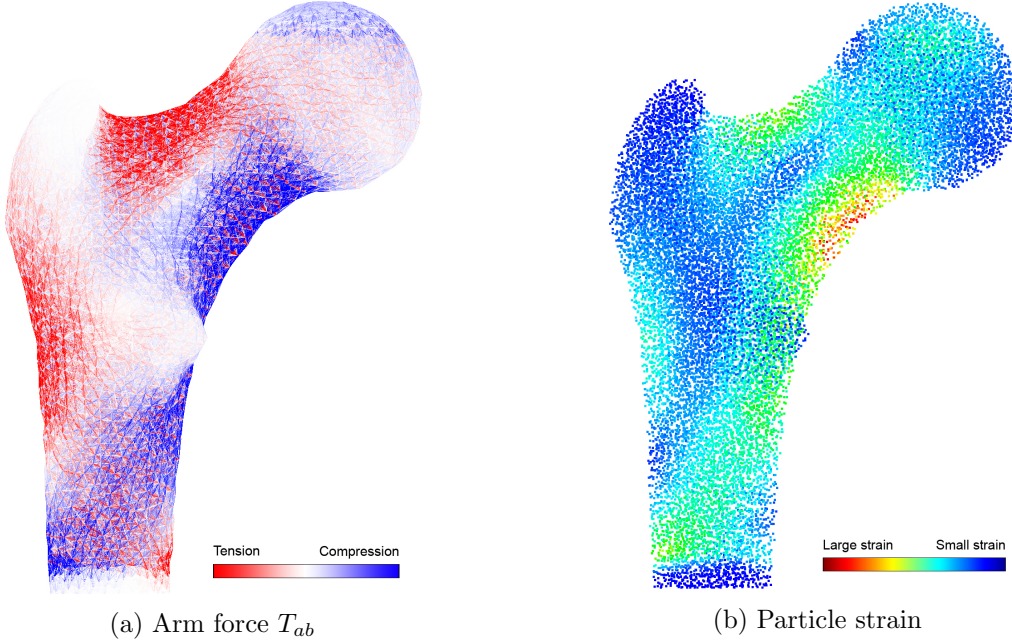(a) Arm force T_{ab}

(b) Particle strain

Figure 7: Analysis results for the 3D femur prior to stiffness scaling. The compression and tension is concentrated to the outer most fibres as expected in a bending situation.
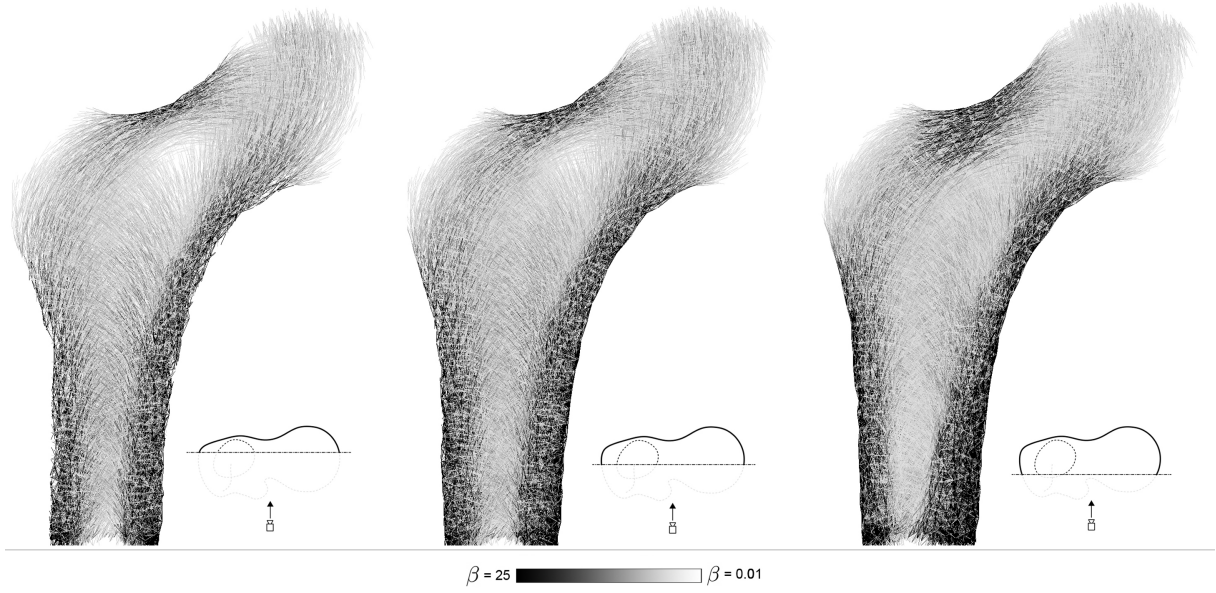
9

Figure 8: Three sections through the femur bone where the arms are colored by the stiffness scaling factor β. A large scale factor is black and a small scale factor is white. 5% of the least strained arms (which would have been white) have been removed in the visualisation so that the other arms appear more clearly.

4.3 Structural frame

A structural frame in 2D which is exerted to a uniform distributed load case is modelled using 24840 particles and 675939 arms, for $\alpha = 5.5$. Figure 9 show the setup and Figure 10 the results from the analysis prior to the stiffness scaling. The results from the stiffness scaling is illustrated in Figure 11 where two different stiffness adaptations are run, one for $\beta_{max} = 5$ and one for $\beta_{max} = 25$. The example serves to illustrate how the limits on β has an effect on the results. A smaller β_{max} range mimics a weaker material and a smaller β_{min} results in more removed material.

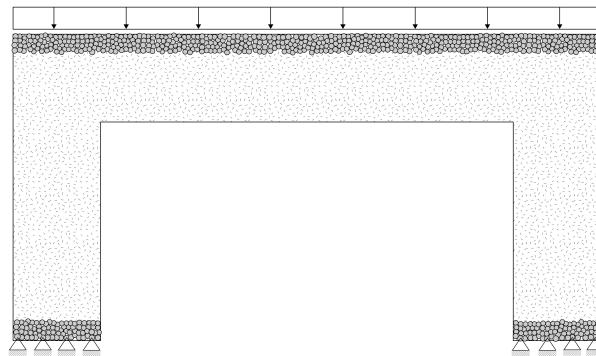

Figure 9: A 2D frame which is locked with moment connections at the base and loaded with an evenly distributed load along the top.
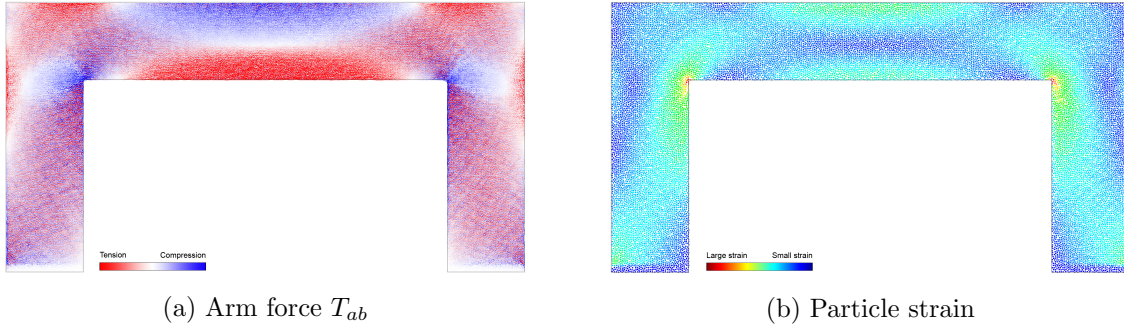
(a) Arm force T_{ab}

(b) Particle strain

Figure 10: Results form analysis prior to stiffness scaling illustrated as tension and compression force in the arms and strain for the particles.
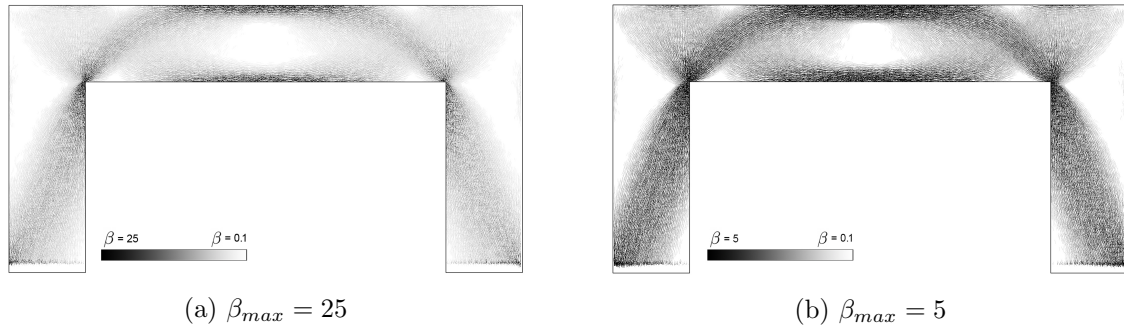

(a) $\beta_{max} = 25$

(b) $\beta_{max} = 5$

Figure 11: The 2D frame where the arms are coloured by the stiffness scale factor β. The left figure have a larger β_{max} compared to the right figure, which can be seen to effect the results with thicker dense areas in figure b).

5 Discussion and Conclusions

The present study exemplified a the use of a simple meshless method for guidance of material placement in structural components and/or creation of patterns for distribution of material density and porosity. The femur bone examples accumulate stiffness in the expected regions with promising results in both 2D and 3D. The frame example also indicate a reasonable behaviour and exemplify how the the change in β_{max} has an impact on the thickness of the more dens areas as one would expect. The presented approach is based on relative values of stiffness and force but real material properties could be implemented in future work. A translation from the meshless analysis results and printable 3D geometry also need to be developed for construction of porous components.

6 Acknowledgements

References

[1]   D. Group. *Digital twin city centre*. URL: https://dtcc.chalmers.se/ (visited on 05/24/2022).

[2]   O. Sigmund and K. Maute. "Topology optimization approaches". In: *Structural and Multidisciplinary Optimization* 48.6 (Aug. 2013), pp. 1031–1055.

[3]   A. G. Weldeyesus et al. "Truss geometry and topology optimization with global stability constraints". In: *Structural and Multidisciplinary Optimization* 62.4 (Aug. 2020), pp. 1721–1737.

[4]   A. Mazurek, W. F. Baker, and C. Tort. "Geometrical aspects of optimum truss like structures". In: *Structural and Multidisciplinary Optimization* 43.2 (Aug. 2010), pp. 231–242.

[5]   W. F. Baker, A. Beghini, and A. Mazurek. "Applications of Structural Optimization in Architectural Design". In: *20th Analysis and Computation Specialty Conference*. American Society of Civil Engineers, Mar. 2012.

[6]   J. Wolff. *The Law of Bone Remodelling*. Springer Berlin Heidelberg, 1986.

[7]   R. Huiskes et al. "Adaptive bone-remodeling theory applied to prosthetic-design analysis". In: *Journal of Biomechanics* 20.11-12 (Jan. 1987), pp. 1135–1150.

[8]   H. E. Pettermann, T. J. Reiter, and F. G. Rammerstorfer. "Computational simulation of internal bone remodeling". In: *Archives of Computational Methods in Engineering* 4.4 (Dec. 1997), pp. 295–323.

[9]   A. Sadegh, G. Luo, and S. Cowin. "Bone ingrowth: An application of the boundary element method to bone remodeling at the implant interface". In: *Journal of Biomechanics* 26.2 (Feb. 1993), pp. 167–182.

[10] M. Bagge. "A model of bone adaptation as an optimization process". In: *Journal of Biomechanics* 33.11 (Nov. 2000), pp. 1349–1357.

[11] P. Fernandes, J. Guedes, and H. Rodrigues. "Topology optimization of three-dimensional linear elastic structures with a constraint on "perimeter"". In: *Computers & Structures* 73.6 (Dec. 1999), pp. 583–594.

[12] K. M. Liew, H. Y. Wu, and T. Y. Ng. "Meshless method for modeling of human proximal femur: treatment of nonconvex boundaries and stress analysis". In: *Computational Mechanics* 28.5 (May 2002), pp. 390–400.

[13] R. A. Gingold and J. J. Monaghan. "Smoothed particle hydrodynamics: theory and application to non-spherical stars". In: *Monthly Notices of the Royal Astronomical Society* 181.3 (Dec. 1977), pp. 375–389.

[14] S. A. Silling. "Reformulation of elasticity theory for discontinuities and long-range forces". In: *Journal of the Mechanics and Physics of Solids* 48.1 (Jan. 2000). Introduction of Peridynamics, pp. 175–209.

[15] J. Olsson, M. Ander, and C. J. K. Williams. "The Use of Peridynamic Virtual Fibres to Simulate Yielding and Brittle Fracture". In: *Journal of Peridynamics and Nonlocal Modeling* 3.4 (Apr. 2021), pp. 348–382.

[16] L. Verlet. "Computer "Experiments" on Classical Fluids. I. Thermodynamical Properties of Lennard-Jones Molecules". In: *Phys. Rev.* 159 (1 July 1967), pp. 98–103.

[17] R. W. Macek and S. A. Silling. "Peridynamics via finite element analysis". In: *Finite Elements in Analysis and Design* 43.15 (Nov. 2007), pp. 1169–1178.

[18] J. J. Monaghan. "Smoothed Particle Hydrodynamics". In: *Annual Review of Astronomy and Astrophysics* 30.1 (Sept. 1992), pp. 543–574.

[19] J. Belinha, L. Dinis, and R. N. Jorge. "The Meshless Methods in the Bone Tissue Remodelling Analysis". In: *Procedia Engineering* 110 (2015), pp. 51–58.